Purdue University
Purdue e-Pubs

Birck and NCN Publications | Birck Nanotechnology Center

1-11-2012

Annealing dependent performance of organic bulk-heterojunction solar cells: A theoretical perspective

Biswajit Ray
Purdue University - Main Campus, ray0@purdue.edu

Pradeep Nair
Purdue University

Muhammad A. Alam
Birck Nanotechnology Center, Purdue University

Follow this and additional works at: http://docs.lib.purdue.edu/nanopub

Part of the Electronic Devices and Semiconductor Manufacturing Commons, and the Power and Energy Commons

Ray, Biswajit; Nair, Pradeep; and Alam, Muhammad A., "Annealing dependent performance of organic bulk-heterojunction solar cells: A theoretical perspective" (2012). *Birck and NCN Publications.* Paper 853.
http://docs.lib.purdue.edu/nanopub/853

This document has been made available through Purdue e-Pubs, a service of the Purdue University Libraries. Please contact epubs@purdue.edu for additional information.

Solar Energy Materials & Solar Cells 95 (2011) 3287–3294

Contents lists available at ScienceDirect

Solar Energy Materials & Solar Cells

journal homepage: www.elsevier.com/locate/solmat

Annealing dependent performance of organic bulk-heterojunction solar cells: A theoretical perspective

Biswajit Ray*, Pradeep R. Nair, Muhammad A. Alam

School of Electrical and Computer Engineering, Purdue University, West Lafayette, IN 47906, USA

ARTICLE INFO

Article history:
Received 11 March 2011
Received in revised form
6 July 2011
Accepted 11 July 2011

Keywords:
Annealing
Morphology
Organic solar cell
Process conditions

ABSTRACT

Organic photovoltaic (OPV) technology promises a relatively inexpensive option for the solar energy conversion, provided its efficiency increases beyond the current level (~7–8%) along with significant improvement in operational lifetime. To achieve this high efficiency/reliability, a systematic theoretical approach is required to optimize the underlying device fabrication process. In this article, we use an anneal-time dependent process-device co-simulation framework (the phase-field model for phase separation coupled with the self-consistent drift-diffusion transport for free carriers) to explore the effects of the process conditions (e.g., annealing temperature, anneal duration) on the performance of organic solar cells. Our results explain experimentally observed annealing effects on the solar cell performance, namely, (i) peak of the short circuit current, (ii) insensitivity of the open circuit voltage, (iii) low fill factor, etc., that would otherwise be deemed anomalous from the perspective of conventional solar cells. As such, this work offers a detailed analysis of the effects of annealing on OPV morphology and its electrical performance. This work also provides a theoretical framework for the optimization of process conditions, which might eventually lead to higher efficiency/reliability of the organic photovoltaic technology.

Published by Elsevier B.V.

1. Introduction and background

The low-temperature, solution-based, inexpensive manufacture [1] of the organic solar cell makes it a promising alternative to the classical photovoltaic technologies based on crystalline and amorphous silicon. As the low-temperature process is also compatible with flexible light-weight substrates such as plastics, organic photovoltaic (OPV) technology reduces installation cost and would conform to novel, non-traditional surfaces [2]. These well known advantages of economic processing, however, are offset by equally well known issues of poor efficiency [3–5], high process sensitivity [6,7], and rapid performance degradation at the operating conditions [8]. Many research groups are exploring various material systems to improve the performance and stability of OPV, but, irrespective of the material choice, optimization of the fabrication process remains a key challenge for the success of OPV technology.

Performance of the bulk heterojunction (BHJ) type OPV critically depends on various process parameters [6,7] such as the blending ratio of donor (D) and acceptor (A) materials, the solvent in which they are mixed, the annealing conditions (anneal time and temperature) of the solution, etc. In the last few years, a number of experiments have tried to systematically deconvolve the effect of the each process variable on the ultimate efficiency of the cell [6,7]. These experiments show that the cell performance is highly sensitive to the anneal duration [9–12]. Moreover, careful physical characterizations (optical microscopy, small and wide angle XRD, TEM images) [13,14] show that change in annealing conditions significantly alters the nature of the underlying active layer morphology, and the morphology is correlated to the cell performance. Recently many experiments [6,7,9–12] have systematically explored the optimum anneal condition for specific material systems. Thus, the importance of annealing in the fabrication of OPV is well established, but still there is no theoretical framework to explore its effects for a generic material system. Indeed, there remain many unanswered questions regarding the time evolution of the various solar cell parameters (short circuit current (J_{SC}), open circuit voltage (V_{OC}), fill factor (FF)) during the annealing process [6,7,9–12]. One such puzzling aspect, common to many reports in the literature, is the insensitivity of the open circuit voltage with annealing, even though J_{SC} varies significantly with anneal duration [6,7,9–12] (see Fig. S1 in the Supplementary material).

From the theoretical side, there has been significant progress over the last few years on the transport simulation of the BHJ

* Corresponding author.
E-mail addresses: biswajit.025@gmail.com (B.R. Ray), alam@purdue.edu (M.A. Alam).

0927-0248/$ - see front matter Published by Elsevier B.V.
doi:10.1016/j.solmat.2011.07.006

solar cell. Koster et al. [15] modeled the transport and recombination in the BHJ-OPV using a 1D homogenized effective media approach. This approach was later extended for the transport simulation in 2D disordered device structure of BHJ solar cell [16,17]. With regard to the process-device co-modeling, several groups have explored the effect of nano-morphology on the performance of solar cell by cellular automata approach [18–20]. While these studies sensitize the community of the importance of morphology on solar cell performance, none of these works explicitly correlate the process conditions, such as anneal time and temperature, to the time evolution of morphology and hence cannot predict the anneal-time dependent device performance. Recently, Buxton and Clarke [17] reported detailed device simulation on a phase-segregated morphology of BHJ solar cells. They simulated the phase-segregated morphology of di-block copolymer solar cells using the Flory–Huggins free energy within the Cahn–Hilliard formalism. Drift-diffusion equations were solved on the meso-structure so created to obtain the *I–V* characteristics. The key focus of their study was the relative performance improvement as the morphology evolves from random to ordered geometry. However, the question of time evolution of morphology during annealing and its effect on the subsequent device performance remain generally unexplored.

Although fabrication of ordered structures for OPV devices is an active area of research [21–23], tailoring the morphology through process conditions like annealing time and temperature remains the key for improving the efficiency of the traditional solution-processed BHJ-OPV. In this context, we generalize the work of Buxton and Clarke [17] to develop a computational framework that connects various process variables to the device characteristics so that the performance of the solar cell is optimized and its efficiency is improved. Using the process model, we first explain the systematic evolution of the active layer morphology as a function of anneal duration (Fig. 2). We also uniquely characterize the morphology by two geometric parameters: interface width (W_{it}) and average domain size (W_C) and discuss their influence on the device characteristics. Second, using the process-device co-simulation, we study the effects of anneal duration on the cell performance (J_{SC}, V_{OC} and *FF*). This analysis allows us to explain the insensitivity of V_{OC} with anneal duration, even as J_{SC} decreases rapidly with longer annealing (see Fig. S1 in the Supplementary material for a summary of reported experiments). Third and finally, we explain that annealing beyond the optimum duration (t_{opt}) degrade the output current significantly, and this non-optimal annealing has direct implication on the intrinsic reliability of OPV cells.

The paper is organized as follows: We first describe the device structure and the working principle of OPV. Next, the process and device modeling approaches are described. The process-device simulation framework is then applied (Section 4) to study the anneal time dependence of the current–voltage characteristics, short circuit current, open circuit voltage, fill factor, etc. Finally, we discuss the optimization of annealing conditions and the intrinsic reliability of the OPV cell.

1.1. Morphology and working of OPV

The schematic of an OPV cell, shown in Fig. 1, indicates that the organic solar cell is morphologically distinct from the conventional, single-crystalline or thin-film (e.g., a-Si, CIGS, or CdTe) solar cells. The conventional solar cell operates as a vertical PN (or PIN) junction diode with stacked layers of p and n doped regions. Instead, for the OPV cells, the interface between the two interpenetrating organic semiconductors (called electron donor (D) and electron acceptor (A)) is neither vertical nor lateral, but is randomly dispersed throughout the volume of cell (hence the term bulk heterojunction (BHJ)). Moreover, unlike classical solar cells, both the donor and the acceptor materials of an OPV cell are simultaneously connected to the top and the bottom electrodes, making it necessary that the anode and cathode electrodes have different work functions for the collection of charge carriers by the respective contacts. In addition, blocking layers [24] are often used so that the carriers cannot escape through the wrong contact.

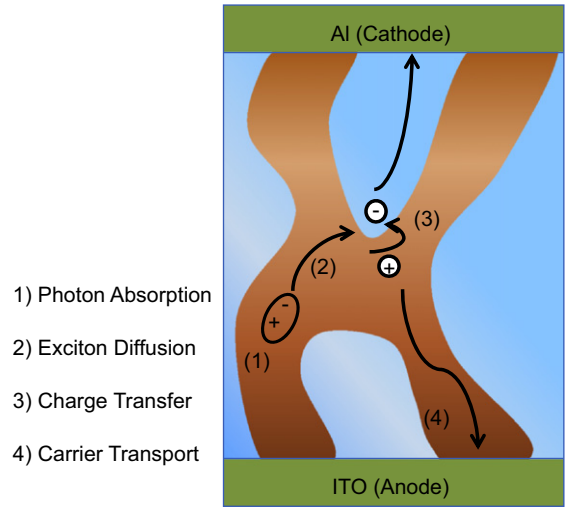

Fig. 1. Schematic of donor/acceptor bulk heterojunction solar cell. The blue region is the acceptor phase (PCBM) and the brown region is the donor phase (P3HT). Excitons (denoted by an oval with + and − sign) are generated in the polymer and they separate into free charges at the interface. Charge carriers are denoted by circles with minus sign for electron and plus for hole. (For interpretation of the references to color in this figure legend, the reader is referred to the web version of this article.)

To appreciate the importance of complex morphology of OPV cells, let us briefly review the four well-known sequential processes defining the electrical operation of the BHJ solar cell (Fig. 1). First, when the photon transmits through the substrate and the electrode (TCO), it is absorbed in the active layer consisting of the D–A blend, generating a strongly bound electron–hole pair ($E_b \sim 0.1-1\,\text{eV}$) called exciton. Next, these excitons diffuse within the disordered active layer morphology defined by respective phases: if they find the donor/acceptor interface within its diffusion length ($L_{ex} = \sqrt{D_{ex}\tau_{ex}} \approx 5-10\,\text{nm}$), they are dissociated into free charge carriers by the quasi-electric field at the heterojunction (step 3 in Fig. 1); otherwise, the excitons are irreversibly lost to self-recombination with corresponding reduction in PV efficiency. Therefore, the distributed donor/acceptor interface is the key innovation of BHJ-OPV because regardless of the origin of an exciton within the active volume, the exciton finds the distributed interface within the diffusion length (L_{ex}) so that they may be dissociated into free charge-carriers with very high probability. After exciton dissociation, electrons are transferred to the acceptor material, while holes remain in the donor region. Once electrons and holes are spatially separated, in the fourth and final step, the built-in electric field (created by the difference in work functions of the front and back electrodes) sweeps the free electrons and holes to the respective contacts, and eventually to the load connected to the solar cell (step 4 in Fig. 1). Note that unlike the beneficial role in exciton dissociation, the complexity in the morphology has a detrimental effect on the electron/hole collection efficiency. *Thus, the performance of the solar cell is dictated by the counter-balancing impact of the active layer morphology on exciton dissociation and charge transport*. Therefore, it has always been a challenge to find the optimum process conditions that ensure the maximum efficiency of the cell.

2. Process model

Spin coating is a popular film forming technique for the fabrication of the bulk heterojunction type organic solar cells. In this technique, the donor and the acceptor materials are mixed with solvent and the solution is then applied to a rotating substrate. The film is then thermally annealed so that the solvent is evaporated out and the phase segregated interpenetrating structure emerges within the D–A mixture. The important process variables that affect the shape/structure of this phase segregated nano morphology are anneal temperature, anneal time, mixing ratio of the D–A molecules, nature of the solvent, etc. These process variables dictate ultimate cell performance by controlling the morphology of the phase-segregated D–A blend. Therefore, it is important to model the morphology as a function of process variables systematically and comprehensively.

2.1. Phase field approach to model phase separation

The time evolution of the active layer morphology depends on the phase separation kinetics of donor–acceptor blend, which is modeled here by the Cahn–Hilliard (C–H) equation [25] as given below

$$\frac{\partial \phi}{\partial t_a} = M_0\left(\nabla^2 \frac{\partial f}{\partial \phi} - 2\kappa\nabla^4\phi\right). \tag{1}$$

Based on the minimization of the total energy, C–H equation evaluates the change of local composition ($\phi(x,y,x,t)$) with anneal time. The first term on the right hand side of Eq. (1) depends on the free energy of mixing (f), and the second term accounts for the surface tension effect due to the formation of the diffused interface [27]. The material specific parameters in Eq. (1) are M_0, the effective mobility parameter (dictated by nature of solvent and the anneal temperature T) and κ, the gradient energy coefficient. The free energy (f) term in Eq. (1) can be modeled by the Flory–Huggins mean field theory [26] as follows

$$f = \frac{k_B T}{v_{site}}\left[\frac{\phi\ln(\phi)}{N_D} + \frac{(1-\phi)\ln(1-\phi)}{N_A} + \chi\phi(1-\phi)\right]. \tag{2}$$

Here v_{site} is the volume of the reference site in the Flory–Huggins lattice model, N_D and N_A are the relative sizes of donor and acceptor molecules, respectively and χ is the enthalpy interaction parameter, also known as Flory mixing parameter. The composition term, ϕ, defines the morphology and its value varies between zero (acceptor molecule) and one (donor molecule). The values for the model parameters in Eq. (1) and (2) are given in Table 1. These parameters can be accurately determined experimentally for a given donor/acceptor material [28,29]. Note that our approach mirrors that of Buxton and Clarke [17] except that we explicitly retain the anneal time (t_a) evolution of the process dynamics. The basic free energy function described above can be generalized to include the effects of the substrate strain, elasticity or the solvent evaporation, multi-component phase-segregation, etc. by appropriately modifying the free energy function [29]. For the broad class of BH solar cells, however, this simple form of free energy (Eq. (2)) provides the essential description of the evolution of morphology as a function of process conditions.

We solve the time dependent C–H (Eq. (2)) equation on an $80\times80\times80$ 3D grid with zero-flux boundary conditions. The initial condition for Eq. (1) is defined by $\phi(t_a=0)\sim0.5$; denoting a random composition fluctuation in a homogenized D–A mixture. Spectral method is used to solve the C–H equation (details of numerical implementation are described in the literature [29]).

3. Device model

For a given morphology of the active layer, the steady state current–voltage (I–V) characteristic of the cell is calculated by solving the following set of coupled equations [16,17]:

Exciton transport:

$$D_{ex}\nabla^2 n_{ex} = G_{ex}(r) - R_{ex}(n_{ex}), \tag{3}$$

Poisson's equation:

$$\nabla(\varepsilon_r\varepsilon_0\nabla\psi) = -q(n_h - n_e), \tag{4}$$

and electron–hole transport:

$$\nabla(\mu_{e,h}n_{e,h}(-\nabla\psi) \pm D_{e,h}\nabla n_{e,h}) = \mp(G_{e,h}(n_{ex}) - R_{e,h}(n_e,n_h)). \tag{5}$$

The transport equations are based on well-known drift-diffusion formalism and have previously been used for OPV in Refs [16,17]. In Eq. (3) $n_{ex}(r)$ is the exciton density (cm^{-3}) at the point $r\equiv(x,y,z)$ of the active layer morphology, D_{ex} is microscopic exciton diffusion constant. Exciton generation (G_{ex}) is considered only in the donor material with a uniform spatial distribution, and the exciton self-recombination term is modeled as $R_{ex}=n_{ex}/\tau_{ex}$, where τ_{ex} is the exciton lifetime in the organic material. In Eqs. (4) and (5) subscript 'h' stands for hole while subscript 'e' denotes electron, ψ is the electrostatic potential, ε_r is the relative dielectric constant for organic materials, $n_{e,h}$ is carrier density, $\mu_{e,h}$ is carrier mobility, $D_{e,h}$ is carrier diffusivity, $G_{e,h}$ is the (free) carrier generation rate, and $R_{e,h}$ is (free) carrier recombination rate. The positive sign in Eq. (5) denotes the electron current and the negative sign is for the hole current. The generation of electron and hole ($G_{e,h}$) is calculated from the exciton flux at the D/A interface, assuming that the probability of exciton dissociation at the D–A interface is unity. The recombination of charge carriers is modeled as $R_{e,h}=\gamma(n_e(s)n_h(s)-n_{int}^2(s))$, where, $s(x,y)$ stands for the points on the interfacial surface of the donor/acceptor region, $n_{int}=N_c\exp(-E_{gap}/2\mathrm{kT})$ is the intrinsic carrier concentration at the interface, $E_{gap}=\mathrm{LUMO}_A-\mathrm{HOMO}_D$ and γ is the recombination strength. The boundary conditions for the set of equations at the electrodes are obtained from the equilibrium carrier concentrations. We assume cathode is grounded and a positive voltage is applied at anode. For all other open boundaries, we assume a zero-flux boundary condition.

3.1. Implementation and validation

We adopt the finite difference method along with the well-known Scharfetter–Gummel's discretization scheme [30] to solve the drift-diffusion equations. We find that the electric field in the device remains essentially constant and is given by $E_z=(V_{bi}-V)/T_{film}$; where V_{bi} is the built-in potential, V is the applied voltage, and T_{film} is the active layer thickness. The assumption of the constant electric field is justified because the intrinsic nature of the organic semiconducting materials suggests that the solution of the Poisson's equation remains essentially linear. In general, the active layer may contain electrically floating islands trapped within the companion phase (see Fig. 2(a–c)) and these islands will not contribute to the steady state output current. Hence, once we simulate the active layer morphology, we identify the regions that are electrically connected to the correct electrode through a percolating network of uninterrupted paths, and solve the carrier transport equations numerically only in these regions.

4. Results and discussion

Given the simulation infrastructure, we explore the performance of the cell as a function of the process conditions, more

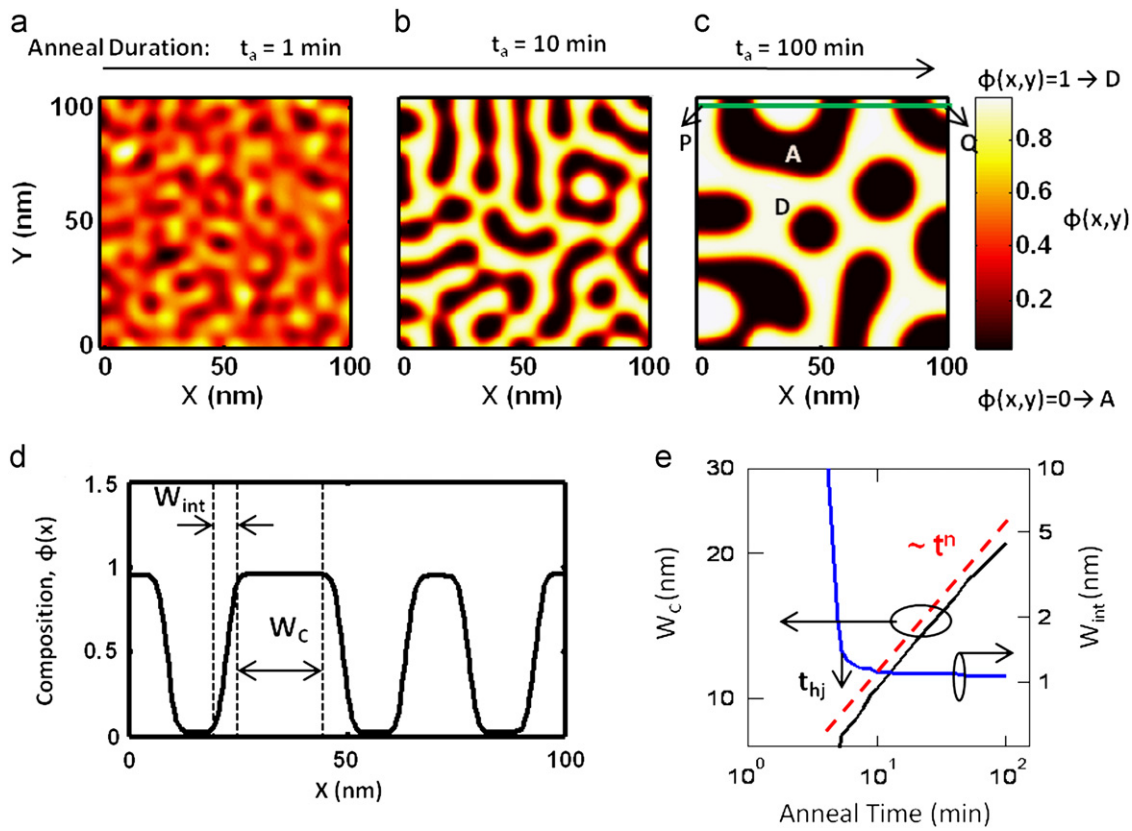

Fig. 2. Morphology evolution with anneal duration. (a–c) Top view of the morphology of the active layer corresponding to three different anneal time. The dark regions in the figure is for acceptor phase ($\phi=\phi_A\sim0$) and the bright regions is for donor phase ($\phi=\phi_D\sim1$). (d) The concentration variation along the 1D cut PQ (the green line in Fig. 1c) is plotted. Here W_{it} is the interfacial width and W_c is the average cluster size. (e) The growth of the average domain size (W_C) with the stress time is plotted (log–log plot). The straight line dependence in the log–log plot indicates that W_C follows a power law with stress time. The evolution of the diffuse interface (W_{int}) between the two phases is shown in the RHS axes of the figure. The values of the various parameters used to simulate the morphology are listed in Table 1. (For interpretation of the references to color in this figure legend, the reader is referred to the web version of this article.)

Table 1
Process parameters used for simulation.

Parameter	Symbol	Numerical value
Anneal temperature	T	393 K
Flory interaction parameter	χ	0.09
Gradient energy coefficient	κ	10^{-11} J/m
Effective polymer mobility	M_0	10^{-26} m^5 J^{-1} s^{-1}
Donor volume fraction	η_D	0.5
Volume of the reference site	v_{site}	10^{-29} m^3
Relative sizes of donor, acceptor molecules	N_D, N_A	33

specifically anneal duration. While our analysis is applicable to any D–A material system, here we use typical model parameters that correspond to P3HT:PCBM system (Tables 1 and 2) to capture the general trends applicable to a broad class of BHJ solar cell.

4.1. Time evolution of morphology

Fig. 2(a–c) shows the morphology evolution of the phase segregated BHJ active layer with anneal duration, obtained by numerical solution of the C–H equation. The figure illustrates that the annealed morphology contains two distinct phase-segregated regions, namely, the donor phase (defined by $\phi=\phi_D\sim1$) and the acceptor phase ($\phi=\phi_A\sim0$). The exact values of ϕ_A and ϕ_D depend on the details of the free energy function. There are many experimental evidences [13,31] based on TEM and optical microscopy images that corroborate such 'anneal time dependent' evolution of morphology. We capture the essential features of the morphology by two effective parameters: interface width (W_{it}) and average domain size (W_c). Later we will show that the influence of annealing on the device performance can be intuitively explained as a function of these two parameters (W_c, W_{it}). Based on Fig. 2(a–c) it appears that the geometry of the mesostructure lacks any specific order/shape, and yet we find that it can be characterized by an average domain width, $W_C(t_a)$, that increases systematically with anneal time t_a (that eventually leads to Ostwald ripening). We also find that the interface between the donor and the acceptor phases is diffuse in nature with a finite width. The width of the diffuse interface ($W_{int}(t_a)$) is defined by the region having composition variation between ϕ_A and ϕ_D. Both W_C and W_{int} are crucial in determining the device performance, and hence they are explicitly defined in Fig. 2(d) with a 1D cut of the actual morphology. In Fig. 2(e) we show that the time evolution of W_{int} saturates to a fixed width ($\sim$1 nm), once the initial stage of phase segregation is complete. We also find that the growth of $W_C(t_a)$ with anneal duration follows a power law (refer to Fig. 2(e)) that stabilizes with constant power-exponent within minutes of the initiation of phase separation. This power law is given by the well-known Lifshitz–Slyozov law [32] of phase-segregated D–A blend, i.e.,

$$W_C(t_a)\sim[D_{eff}t_a]^n. \tag{6}$$

Experimentally, the characteristic length scale of W_C is interpreted as the inverse of the peak-vector (q_{max}) from the light-scattering experiments [14], i.e. $W_C\sim2\pi/q_{max}$. Many groups have reported this anneal time dependent cluster growth (power law (6)) for

Table 2
Device dimensions and transport parameters used for simulation.

Parameter	Symbol	Numerical values
Active layer thickness	T_{film}	80 nm
Exciton diffusion length	L_{ex}	5 nm
Exciton generation rate (in donor)	G_{ex}	$3\times10^{22}\,cm^{-3}\,s^{-1}$
Electron mobility	μ_e	$5\times10^{-4}\,cm^2\,V^{-1}\,s^{-1}$
Hole mobility	μ_h	$10^{-3}\,cm^2\,V^{-1}\,s^{-1}$
Recombination strength	γ	$10^{-9}\,cm^3/s$
Lowest unoccupied molecular orbital (donor)	$LUMO_D$	3.0 eV
Highest occupied molecular orbital (donor)	$HOMO_D$	4.9 eV
Lowest unoccupied molecular orbital (acceptor)	$LUMO_A$	3.7 eV
Highest occupied molecular orbital (acceptor)	$HOMO_A$	6.1 eV
Effective density of states ($HOMO_D$,$HOMO_A$,$LUMO_D$,$LUMO_A$)	N_C	$10^{21}\,cm^{-3}$
Cathode work function (Al)	Φ_c	3.9 eV
Anode work function (ITO)	Φ_a	4.7 eV

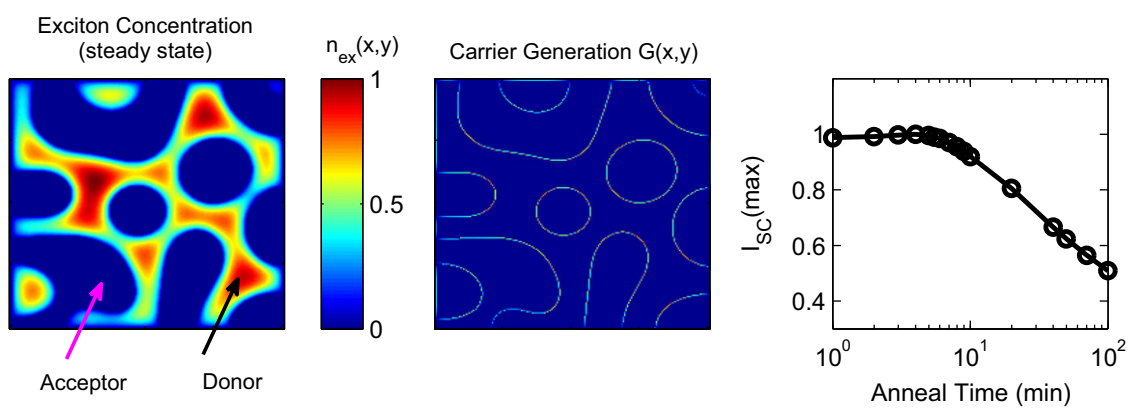

Fig. 3. Effect of annealing on exciton concentration and its dissociation. (a) The steady state exciton concentration (n_{ex}) in the phase-segregated morphology is shown by color-coding. Dark blue regions of the figure are the acceptor phase where we assume no exciton is generated. (b) Spatially distributed electron/hole pair generation, $G_{e-h}(s)$, is shown by the bright spots. Since exciton dissociates only at the interfacial regions, charges carriers are generated only along those interfacial boundary lines. (c) The steady state value of maximum short circuit current, I_{SC}(max) is plotted against anneal time after normalizing the current by total exciton generation rate. With higher anneal duration the morphology coarsens and hence I_{SC}(max) decreases. (For interpretation of the references to color in this figure legend, the reader is referred to the web version of this article.)

polymer: fullerene material system [13], which also validates the numerical implementation of the process model.

4.2. Time evolution of exciton dissociation

For a given morphology, the solution of the transport Eqs. (3)–(5) allows us to evaluate the distribution of carrier (exciton, electron and hole) densities throughout the device. Fig. 3(a) shows the exciton density and the corresponding exciton dissociation profile for a given D/A morphology. Exciton dissociation leads to the generation of charge carriers ($G_{e-h}(s)$), which takes place only at the interfacial nodes. Fig. 3(b) shows a 2D plot of the spatially distributed generation rate of charge carriers. We numerically integrate this carrier generation rate at every grid point of the D/A interfacial surface throughout the volume of the cell to calculate the total exciton current, denoted as I_{SC}(max). Note that this is the maximum limit of the short circuit current for a given morphology; the loss mechanisms (e.g., interfacial recombination, floating island, etc.) will reduce the output current and are considered later in the paper. The steady state values of I_{SC}(max) are plotted in Fig. 3(c) as a function of anneal duration. We find that while I_{SC}(max) varies little at the initial phase of annealing, it decreases rapidly for the morphologies corresponding to higher anneal duration. This transition reflects the coarsening of the morphology beyond the exciton diffusion length: with $W_C(t_a) < L_{ex}$, essentially all the excitons are harvested at the D/A interface and the response is independent of anneal time. On the other hand, for $W_C(t_a) > L_{ex}$, increasingly larger fraction of excitons are lost to self-recombination before they can reach the donor–acceptor interface, and the exciton collection is rapidly reduced.

4.3. Optimum anneal time for J_{SC}

The complete current–voltage (I–V) characteristics for a given morphology, is simulated by solving Eqs. (3)–(5) self-consistently. In Fig. 4(b) we plot the I–V characteristics for four different morphologies with increasing anneal times ($t_a = 4,10,20,100$ min) (The related electron–hole distribution inside the D–A regions are shown in Supplementary material, Section 2). We find that the trends in the I–V curves are similar to the measured I–V characteristics (see Fig. 4(a)) as reported by Zeng et al. [9]. We note that while the short circuit current increases rapidly during initial phase of annealing, its magnitude reduces after an optimum anneal time. The results from our numerical simulation (see the full I–V characteristics in Fig. 4(b)) – obtained using the process-device co-simulation framework – accurately captures this nontrivial anneal-time dependent reversal of the short-circuit current.

To illustrate the variation of short circuit current as a function of anneal time, we plot the value of J_{SC} obtained by numerical simulation on a number of morphologies corresponding to different anneal times in Fig. 5(b). This plot of J_{SC} clearly shows that there is an optimum anneal time, which gives maximum short circuit current. Remarkably, the short-circuit current is low in the initial phase of annealing despite highly efficient exciton harvest (see Fig. 3c). This is because in the initial phase of annealing, the

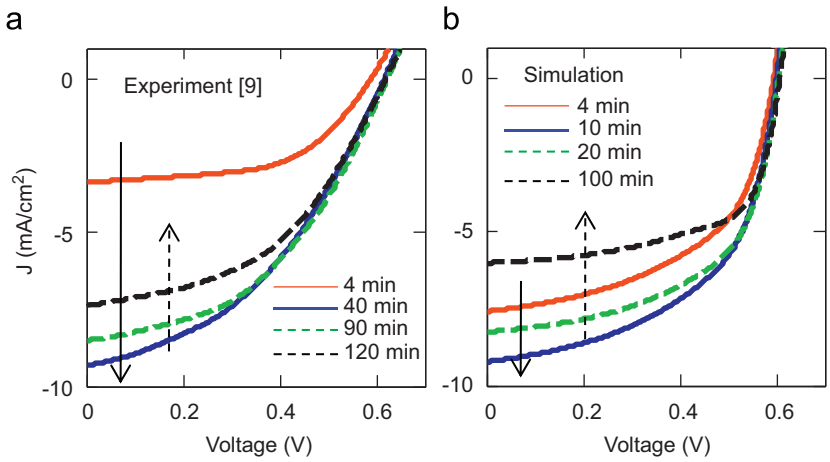

Fig. 4. *I–V* characteristics corresponding to various anneal duration observed in the experiment (a) as well as in simulation (b). Note the similar trend (increase and decrease in current) of the anneal time dependent *I–V* in both experiment and simulation. The transport parameters are listed in Table 2.

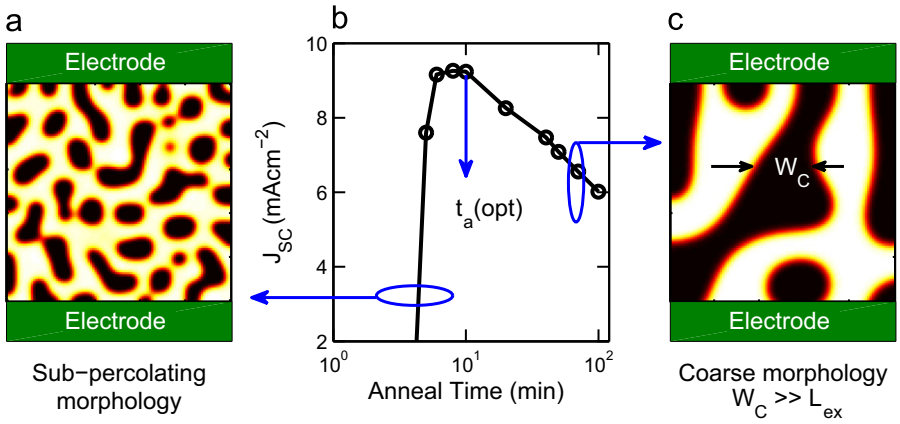

Fig. 5. Effect of annealing on short circuit current. (a) Simulated morphology corresponding to early anneal duration. We see a lot of floating islands in the morphology at the initial phase of annealing. (b) Time evolution of short circuit current (J_{SC}) during annealing for organic solar cell. (c) Coarse morphology corresponding to the late phase of annealing.

morphology consists of many electrically isolated islands (Fig. 5a), which cannot contribute to J_{SC}. Therefore, even though these floating islands may be able to dissociate excitons efficiently (hence high exciton current as shown in Fig. 3c), the resulting electron–hole pairs cannot come out of the cell due to the lack of percolating pathways to the correct electrode. On the other hand, J_{SC} is also reduced at longer anneal times due to coarsening of the morphology (Fig. 5c), which reduces exciton collection, as discussed in Section 4.2. Due to these counter-balancing trends at short and long anneal durations, there exists an optimum anneal time for a given material system and process conditions (see Supplementary material Section 3 for further discussion). The existence of such optimum anneal time for the maximum short circuit current has been experimentally confirmed by many groups [6,7,9–12] (refer to the Fig. S1 of Supplementary material). Although the exact comparison between theory and experiment is difficult as the details of fabrication vary from experiment to experiment, nonetheless, our work provides the theoretical foundation for these experimental observations, and can be used to predict optimum anneal time for a given combination of blend ratio, size of D–A molecules, anneal temperature, etc.

4.4. Anneal time insensitivity of V_{OC}

The rapid reduction in $J_{SC}(t_a)$ for $t_a > t_{opt}$ might lead one to speculate that the open circuit voltage ($V_{OC}(t_a)$) would correspondingly reduce with prolonged annealing, given the classical formula of $V_{OC} = (kT/q)\ln(1+(J_{SC}/J_0))$. However, it is experimentally observed that V_{OC} remains essentially unchanged with anneal duration (see Refs. [6,7,9–12] and Fig. S1 of Supplementary material for a summary of the experimental results). With the process-device simulation framework, we can now explain this puzzling behavior of V_{OC} (see Fig. 6(a) for the time evolution of V_{OC}). As discussed earlier, the main reason for the reduction in J_{SC} at longer anneal time is the coarsening of the morphology, and a reduction of the D/A interfacial area. However, since the interfacial recombination is the main mechanism for the dark current of the cell, the reverse saturation current (J_0) also reduces proportionally with increasing t_a (see Fig. 6(b)). Therefore, V_{OC} remains invariant with anneal time as the ratio of photo current (J_{SC}) and reverse saturation current (J_0) remains essentially a constant, independent of the coarsening of the morphology. While many of these features have been reported in the literature [6,7,9–12] (and exact anneal time to reach V_{oc} saturation depends on specific experiment), we know of no previous theoretical interpretation of this well-known experimental observation.

4.5. Evolution of fill factor and efficiency with annealing

The Fill factor (*FF*) of a solar cell is defined as $P_{max}/(V_{oc}I_{sc})$, where P_{max} is the maximum power point in the *I–V* characteristics of the cell. It is well known that the fill factor of bulk heterojunction type OPV is generally low, typically in the range of ~0.5–0.6. There is, however, no consensus regarding the effect of annealing on *FF*, as both increasing as well as decreasing trends have been experimentally observed (see Refs. [6,7,9–12] and

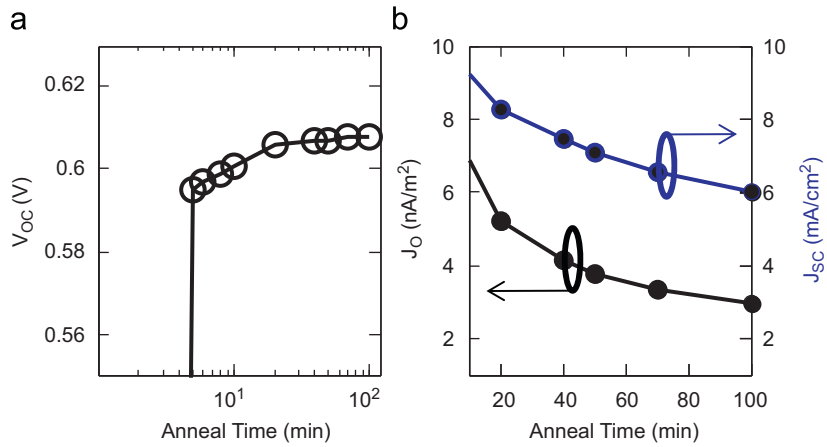

Fig. 6. Effect of annealing on open circuit voltage. (a) Time evolution of open circuit voltage (V_{OC}) during annealing for organic solar cell. (b) Anneal time dependence of reverse saturation current (J_o) and short circuit current (J_{SC}). We see that both the current scales (decreases) proportionally with annealing and hence their ratio remains fixed after certain duration of annealing.

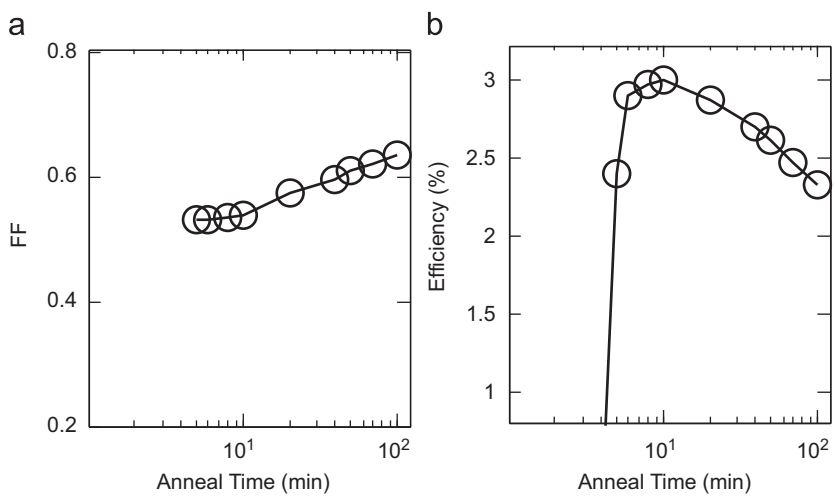

Fig. 7. Effect of annealing on fill factor and efficiency. (a) Time evolution of Fill Factor (FF) during annealing for organic solar cell. (b) Time evolution of the efficiency of organic solar cell as a function of anneal duration.

Fig. S1 of Supplementary material). Our simulation (see Fig. 7a) confirms that low *FF* (0.5–0.6) is a characteristic feature of bulk heterojunction OPV. We also find that the *FF* improves with annealing. We believe that this improvement in *FF* reflects reduced interface recombination (Fig. 6b) associated with coarsening of the film morphology (Fig. 2). However, a quantitative analytical model of *FF* that explicitly relates mobility, interface recombination and anneal time will require further work. Finally, in Fig. 7(b) we plot the efficiency of OPV as a function of anneal duration. Since efficiency$=J_{SC}V_{OC}FF/P_{in}$ (P_{in} is input power $\sim$1 kW/m^2), we note that the efficiency curve mirrors the J_{SC} curve as V_{OC} and *FF* are insensitive to annealing. Thus, this work offers a quantitative explanation regarding the origin of the optimum anneal time for OPV efficiency reported in the literature.

4.6. Morphology and reliability of OPV

The various degradation mechanisms of OPV are complicated and poorly understood [33–37]. In a recent review article [33], Krebs described several possible degradation issues of OPV, which includes chemical degradation of electrode metals and organic molecules in the presence of oxygen and water [34,35], photo-oxidation of polymers, thermal degradation due to morphological change, etc. Let us now consider the thermal degradation [38] due to morphological change, from the perspective of process-device correlation effects discussed in this paper.

In the device model section we assumed that once the annealing is completed and the process temperature (T_{anneal}) is reduced to operating temperature (T_{op}), the phase segregation may be considered "arrested" during measurement/analysis window. In practice, however, phase segregation continues even at T_{op}, albeit at much lower rate because of reduced diffusion. During the prolonged period of field operation, the feature size of the phase-segregated morphology will continue to coarsen compared to the exciton diffusion length, and as a result, exciton harvesting (and the short circuit current) will reduce with time. This continued phase segregation at operating conditions has inherent implications on the lifetime of the BHJ solar cell. Indeed, many experimental observations in the literature [31,38,39] strongly suggest that this time dependent degradation process of the BHJ solar cell (at various stress temperature) is an essential feature of performance degradation. The rate of the degradation depends on the operational temperature, as the kinetics of the phase separation is a temperature-activated process (see Eqs. (1) and (2)). The process-device simulation framework described in this work is well equipped to address this thermal degradation issue (as discussed elsewhere, [40]) for this kind of BHJ solar cell.

5. Conclusion

In summary, we have developed a conceptual and computational framework to connect process conditions to the ultimate device performance for organic solar cells. This framework generalizes the previous work of Buxton and Clarke [17] by explicitly accounting for process conditions like anneal time and temperature, etc. This generalized framework allows us to successfully interpret the effects of annealing on the various performance matrices of solar cell and provides an optimization platform for the annealing step in device fabrication. Although we make no effort to replicate the specific numerical values of a given experiment, the key universal features of various experiments (e.g., insensitivity of V_{OC} even with high interface recombination, sharp rise and fall of J_{SC} with annealing) are successfully interpreted within the modeling framework. Finally, based on the process-device co-simulation framework, we believe that the intrinsic reliability of OPV might be predictable, which anticipates the possibility of performance-reliability co-optimization of OPV design.

Acknowledgement

This material is based upon work supported as part of the Center for Re-Defining Photovoltaic Efficiency Through Molecule Scale Control, an Energy Frontier Research Center funded by the U.S. Department of Energy, Office of Science, Office of Basic Energy Sciences under Award number DE-SC0001085.The computational resources for this work were provided by the Network of Computational Nanotechnology under NSF Award EEC-0228390.

Appendix A. Supporting information

Supplementary data associated with this article can be found in the online version at doi:10.1016/j.solmat.2011.07.006.

References

[1] F.C. Krebs, Fabrication and processing of polymer solar cells: a review of printing and coating techniques, Solar Energy Materials and Solar Cells 93 (2009) 394–412.
[2] J. Yoon, A.J. Baca, S. Park, P. Elvikis, J.B. Geddes, L. Li, et al., Ultrathin silicon solar microcells for semitransparent, mechanically flexible and microconcentrator module designs, Nature Materials 7 (2008) 907–915.
[3] J.D. Servaites, M.A. Ratner, T.J. Marks, Practical efficiency limits in organic photovoltaic cells: functional dependence of fill factor and external quantum efficiency, Applied Physics Letters 95 (2009) 163302–163303.
[4] S.R. Forrest, The limits to organic photovoltaic cell efficiency, MRS Bulletin 30 (2005) 28–32.
[5] M. Scharber, D. Mühlbacher, M. Koppe, P. Denk, C. Waldauf, A. Heeger, et al., Design rules for donors in bulk-heterojunction solar cells—towards 10% energy-conversion efficiency, Advanced Materials 18 (2006) 789–794.
[6] J.A. Renz, T. Keller, M. Schneider, S. Shokhovets, K.D. Jandt, G. Gobsch, et al., Multiparametric optimization of polymer solar cells: a route to reproducible high efficiency, Solar Energy Materials and Solar Cells. 93 (2009) 508–513.
[7] J. Alstrup, M. Jørgensen, A.J. Medford, F.C. Krebs, Ultra fast and parsimonious materials screening for polymer solar cells using differentially pumped slot-die coating, ACS Applied Materials & Interfaces 2 (2010) 2819–2827.
[8] M. Jorgensen, K. Norrman, F.C. Krebs, Stability/degradation of polymer solar cells, Solar Energy Materials and Solar Cells 92 (2008) 686–714.
[9] L. Zeng, C.W. Tang, S.H. Chen, Effects of active layer thickness and thermal annealing on polythiophene: fullerene bulk heterojunction photovoltaic devices, Applied Physics Letters 97 (2010) 053303–053305.
[10] Y. Huang, Y. Liao, S. Li, M. Wu, C. Chen, W. Su, Study of the effect of annealing process on the performance of P3HT/PCBM photovoltaic devices using scanning-probe microscopy, Solar Energy Materials and Solar Cells 93 (2009) 888–892.
[11] H. Kim, M. Shin, J. Park, Y. Kim, Effect of long time annealing and incident light intensity on the performance of polymer: fullerene solar cells, IEEE Transactions on Nanotechnology 9 (2010) 400–406.
[12] M. Campoy-Quiles, T. Ferenczi, T. Agostinelli, P.G. Etchegoin, Y. Kim, T.D. Anthopoulos, et al., Morphology evolution via self-organization and lateral and vertical diffusion in polymer: fullerene solar cell blends, Nature Materials 7 (2008) 158–164.
[13] J. Jo, S. Kim, S. Na, B. Yu, D. Kim, Time-dependent morphology evolution by annealing processes on polymer: fullerene blend solar cells, Advanced Functional Materials 19 (2009) 866–874.
[14] M. Chiu, U. Jeng, C. Su, K.S. Liang, K. Wei, Simultaneous use of small- and wide-angle X-ray techniques to analyze nanometerscale phase separation in polymer heterojunction solar cells, Advanced Materials 20 (2008) 2573–2578.
[15] L.J.A. Koster, E.C.P. Smits, V.D. Mihailetchi, P.W.M. Blom, Device model for the operation of polymer/fullerene bulk heterojunction solar cells, Physical Review B 72 (2005) 085205.
[16] M. Shah, V. Ganesan, Correlations between morphologies and photovoltaic properties of rod-coil block copolymers, Macromolecules 43 (2010) 543–552.
[17] G.A. Buxton, N. Clarke, Predicting structure and property relations in polymeric photovoltaic devices, Physical Review B 74 (2006) 085207.
[18] L. Meng, Y. Shang, Q. Li, Y. Li, X. Zhan, Z. Shuai, et al., Dynamic Monte Carlo simulation for highly efficient polymer blend photovoltaics, The Journal of Physical Chemistry B 114 (2010) 36–41.
[19] B. Lei, Y. Yao, A. Kumar, Y. Yang, V. Ozolins, Quantifying the relation between the morphology and performance of polymer solar cells using Monte Carlo simulations, Journal of Applied Physics 104 (2008) 024504–024506.
[20] K.O. Sylvester-Hvid, S. Rettrup, M.A. Ratner, Two-dimensional model for polymer-based photovoltaic cells: numerical simulations of morphology effects, The Journal of Physical Chemistry B 108 (2004) 4296–4307.
[21] A.A. Gorodetsky, C. Chiu, T. Schiros, M. Palma, M. Cox, Z. Jia, et al., Reticulated heterojunctions for photovoltaic devices, Angewandte Chemie International Edition 49 (2010) 7909–7912.
[22] Z. Fan, H. Razavi, J. Do, A. Moriwaki, O. Ergen, Y. Chueh, et al., Three-dimensional nanopillar-array photovoltaics on low-cost and flexible substrates, Nature Materials 8 (2009) 648–653.
[23] M.D. McGehee, Nanostructured organic–inorganic hybrid solar cells, MRS Bulletin 34 (2009) 95–100.
[24] A.W. Hains, J. Liu, A.B.F. Martinson, M.D. Irwin, T.J. Marks, Anode interfacial tuning via electron-blocking/hole-transport layers and indium tin oxide surface treatment in bulk-heterojunction organic photovoltaic cells, Advanced Functional Materials 20 (2010) 595–606.
[25] J.W. Cahn, Phase separation by spinodal decomposition in isotropic systems, Journal of Chemical Physics 42 (1965) 93–99.
[26] R.A.L. Jones, Soft Condensed Matter, Oxford University Press, Oxford, New York, 2002.
[27] R.W. Balluffi, S.M. Allen, W.C. Carter, R.A. Kemper, Kinetics of Materials, Wiley-Interscience, Hoboken, NJ, 2005.
[28] Y. Shang, L. Fang, M. Wei, C. Barry, J. Mead, D. Kazmer, Verification of numerical simulation of the self-assembly of polymer–polymer–solvent ternary blends on a heterogeneously functionalized substrate, Polymer 52 (2011) 1447–1457.
[29] Y. Shang, D. Kazmer, M. Wei, J. Mead, C. Barry, Numerical simulation of phase separation of immiscible polymer blends on a heterogeneously functionalized substrate, Journal of Chemical Physics 128 (2008) 224907–224909.
[30] D. Scharfetter, H. Gummel, Large-signal analysis of a silicon Read diode oscillator, IEEE Transactions on Electron Devices 16 (1969) 64–77.
[31] S. Bertho, I. Haeldermans, A. Swinnen, W. Moons, T. Martens, L. Lutsen, et al., Influence of thermal ageing on the stability of polymer bulk heterojunction solar cells, Solar Energy Materials and Solar Cells 91 (2007) 385–389.
[32] I. Lifshitz, V. Slyozov, The kinetics of precipitation from supersaturated solid solutions, Journal of Physics and Chemistry of Solids 19 (1961) 35–50.
[33] F.C. Krebs, Degradation and stability of polymer and organic solar cells, Solar Energy Materials and Solar Cells 92 (2008) 685.
[34] K. Norrman, M.V. Madsen, S.A. Gevorgyan, F.C. Krebs, Degradation patterns in water and oxygen of an inverted polymer solar cell, Journal of the American Chemical Society 132 (2010) 16883–16892.
[35] K. Norrman, S.A. Gevorgyan, F.C. Krebs, Water-induced degradation of polymer solar cells studied by $H_2$18O labeling, ACS Applied Materials & Interfaces 1 (2009) 102–112.
[36] S.A. Gevorgyan, A.J. Medford, E. Bundgaard, S.B. Sapkota, H. Schleiermacher, B. Zimmermann, et al., An inter-laboratory stability study of roll-to-roll coated flexible polymer solar modules, Solar Energy Materials and Solar Cells. 95 (2011) 1398–1416.
[37] M.O. Reese, S.A. Gevorgyan, M. Jørgensen, E. Bundgaard, S.R. Kurtz, D.S. Ginley, et al., Consensus stability testing protocols for organic photovoltaic materials and devices, Solar Energy Materials and Solar Cells. 95 (2011) 1253–1267.
[38] B. Conings, S. Bertho, K. Vandewal, A. Senes, J. D'Haen, J. Manca, et al., Modeling the temperature induced degradation kinetics of the short circuit current in organic bulk heterojunction solar cells, Applied Physics Letters 96 (2010) 163301–163303.
[39] B.J. Kim, Y. Miyamoto, B. Ma, J.M.J. Fréchet, Photocrosslinkable polythiophenes for efficient, thermally stable, organic photovoltaics, Advanced Functional Materials 19 (2009) 2273–2281.
[40] B. Ray, M.A. Alam, A compact physical model for morphology induced intrinsic degradation of organic bulk heterojunction solar cell, Applied Physics Letters 99 (2011) 033303-3.